

Chapter 2

Gandalf

2.1 Introduction

We have developed a new code called *Gandalf*^{*} to solve the KRMHD Eqs. (1.16) and (1.19). *Gandalf* is written in CUDA, a GPU computing platform and programming model invented by NVIDIA, and is an efficient numerical tool to study the long-wavelength asymptotic behavior of anisotropic magnetized plasmas.

2.2 Equations

Instead of directly solving Eq. (1.19), we first expand g in Eq. (1.19) (superscripts will be suppressed whenever no confusion would result) in terms of its Hermite moments. Evolving the moments of g instead of using a grid in velocity space makes the numerical scheme spectrally accurate in the v_{\parallel} coordinate. Expanding Eq. (1.19) in terms of Hermite polynomials also provides an elegant analytical framework to study phase mixing (see Chapter 3 for details). The Hermite moments are defined as follows:

$$g(v_{\parallel}) = \sum_{m=0}^{\infty} \frac{H_m(v_{\parallel}/v_{\text{th}})F_0}{\sqrt{2^m m!}} g_m, \quad g_m = \int dv_{\parallel} \frac{H_m(v_{\parallel}/v_{\text{th}})}{\sqrt{2^m m!}} g(v_{\parallel}), \quad (2.1)$$

^{*}The code solves for *g-and-Alfvén* waves, hence the name.

where H_m is the Hermite polynomial of order m . Eq. (1.19) then becomes a fluid-like hierarchy of equations:

$$\frac{dg_0}{dt} + v_{\text{th}} \nabla_{\parallel} \frac{g_1}{\sqrt{2}} = 0, \quad (2.2)$$

$$\frac{dg_1}{dt} + v_{\text{th}} \nabla_{\parallel} \left(g_2 + \frac{(1 - 1/\Lambda)}{\sqrt{2}} g_0 \right) = 0, \quad (2.3)$$

$$\begin{aligned} \frac{dg_m}{dt} + v_{\text{th}} \nabla_{\parallel} \left(\sqrt{\frac{m+1}{2}} g_{m+1} + \sqrt{\frac{m}{2}} g_{m-1} \right) \\ = C[g_m], \quad m \geq 2. \end{aligned} \quad (2.4)$$

The first term on the right hand side of Eq. (1.19), being proportional to H_1 , only appears in Eq. (2.3). The parallel streaming term couples each Hermite moment to the previous and the next moment[†]. Dynamical coupling of different Hermite moments is the mathematical manifestation of linear phase mixing in Hermite space.

The right hand side of Eq. (2.4) has a collision operator $C[g_m]$ that has been added to the kinetic Eq. (1.19). Collisions are included in order to regularize the system at small velocity space scales. More importantly, they are also physically required to generate entropy and heat the plasma—an exactly collisionless limit is unphysical. We choose a convenient collision operator, the Lenard–Bernstein collision operator [80], which in Hermite space looks like:

$$C[g_m] = -\nu m g_m, \quad (2.5)$$

where ν is the collision frequency. The collision operator acts only on the second and

[†]This is a result of the Hermite recurrence relation: $H_{m+1}(v) = 2vH_m(v) - 2mH_{m-1}(v)$.

higher Hermite moments, and hence, conserves particle number and momentum. This particular collision operator is also manifestly most effective for the highest moments retained, since $C[g_m] \propto m$.

Eq. (1.16) and Eqs. (2.2–2.4) are the equations that are implemented in *Gandalf*.

2.3 Normalization

We normalize the perpendicular spatial co-ordinates x, y and the parallel spatial co-ordinate z , to independent arbitrary length scales ρ and L , respectively (with the assumption $L \gg \rho$). By normalizing parallel and perpendicular co-ordinates independently, we can simulate highly anisotropic fluctuations with a numerical box that is roughly a cube. In addition, since the ratio L/ρ is arbitrary, a single run simulates a whole range of problems with varying degrees of anisotropy. Time is normalized to L/v_A . The Elsasser fields ξ^\pm are normalized to ρv_A (gradients of the Elsasser fields have units of velocity—see Eq. (1.17)). The Hermite moments g_m of the perturbed distribution function g are in arbitrary units. The Elsasser fields ξ^\pm , and the distribution function moments g_m are scaled up by a factor of L/ρ so that all normalized terms have unity order of magnitude.

The normalized equations can then be written as,

$$\frac{\partial \nabla_\perp^2 \xi^\pm}{\partial t} \mp \frac{\partial \nabla_\perp^2 \xi^\pm}{\partial z} = -\frac{1}{2} [\{\xi^+, \nabla_\perp^2 \xi^-\} + \{\xi^-, \nabla_\perp^2 \xi^+\} \mp \nabla_\perp^2 \{\xi^+, \xi^-\}], \quad (2.6)$$

$$\frac{dg_0}{dt} + \sqrt{\beta_i} \nabla_{\parallel} \frac{g_1}{\sqrt{2}} = 0, \quad (2.7)$$

$$\frac{dg_1}{dt} + \sqrt{\beta_i} \nabla_{\parallel} \left(g_2 + \frac{1 - 1/\Lambda}{\sqrt{2}} g_0 \right) = 0, \quad (2.8)$$

$$\begin{aligned} \frac{dg_m}{dt} + \sqrt{\beta_i} \nabla_{\parallel} \left(\sqrt{\frac{m+1}{2}} g_{m+1} + \sqrt{\frac{m}{2}} g_{m-1} \right) \\ = -\nu m g_m, \quad m \geq 2, \end{aligned} \quad (2.9)$$

where

$$\frac{d}{dt} = \frac{\partial}{\partial t} + \{\Phi, \dots\}, \quad \nabla_{\parallel} = \frac{\partial}{\partial z} + \{\Psi, \dots\}, \quad (2.10)$$

$$\Phi = \frac{\xi^+ + \xi^-}{2}, \quad \Psi = \frac{\xi^+ - \xi^-}{2}, \quad (2.11)$$

and $\beta_i = 8\pi n_{0i} T_i / B_0^2$ is the ion plasma beta, n_{0i} is the equilibrium ion density, T_i is the equilibrium ion temperature, and B_0 is the magnitude of the background magnetic field.

2.4 Algorithm

We solve Eqs. (2.6–2.9) using a pseudo-spectral scheme. The Elsasser fields ξ^{\pm} , and the Hermite moments g_m are expressed in terms of Fourier modes. The nonlinear term is calculated in the real space by taking fast Fourier transforms using the CUDA FFT library. After transforming back to Fourier space, the nonlinear term is dealiased according to the Orszag 2/3rd dealiasing rule [81]. The time integration for the linear term in Eq. (2.6) is done analytically using an integrating factor technique (discussed below); the nonlinear term is integrated using second-order Runge-Kutta

scheme[‡].

Consider the Fourier transform of Eq. (2.6),

$$\frac{\partial \xi^\pm}{\partial t} \mp ik_z \xi^\pm = \frac{1}{k_\perp^2} [\text{NL}] , \quad (2.12)$$

where $[\text{NL}]$ are all the nonlinear terms. The $k_x = 0, k_y = 0$ mode is decoupled from all the other Fourier modes, and is not included in our simulations. Multiply throughout by $e^{-ik_z t}$,

$$\frac{\partial (\xi^\pm e^{\mp ik_z t})}{\partial t} = e^{\mp ik_z t} \frac{1}{k_\perp^2} [\text{NL}] . \quad (2.13)$$

Eqs. (2.13) and (2.4) are then discretized in time and solved as follows:

1. Take a half time-step:

$$\xi^{\pm, n+1/2} = e^{\pm ik_z \delta t / 2} \xi^{\pm, n} + e^{\pm ik_z \delta t / 2} \frac{1}{k_\perp^2} [\text{NL}]^n , \quad (2.14)$$

$$g_0^{n+1/2} = g_0^n - \frac{\delta t}{2} \left[\{\Phi^n, g_0^n\} + \frac{ik_z \sqrt{\beta_i}}{\sqrt{2}} g_1^n + \sqrt{\beta_i} \left\{ \Psi^n, \frac{g_1^n}{\sqrt{2}} \right\} \right] , \quad (2.15)$$

$$\begin{aligned} g_1^{n+1/2} = g_1^n - \frac{\delta t}{2} & \left[\{\Phi^n, g_1^n\} + ik_z \sqrt{\beta_i} \left(g_2^n + (1 - 1/\Lambda) \frac{g_0^n}{\sqrt{2}} \right) \right. \\ & \left. + \sqrt{\beta_i} \left\{ \Psi^n, \left(g_2^n + (1 - 1/\Lambda) \frac{g_0^n}{\sqrt{2}} \right) \right\} \right] , \end{aligned} \quad (2.16)$$

[‡]This choice was made for ease of numerical implementation, and due to memory constraints on the GPU. The unconditionally unstable nature of RK2 is mollified by choosing a small time-step. The RK2 time-stepping scheme can be easily improved upon, which we hope to do in the near future.

$$g_m^{n+1/2} = g_m^n - \frac{\delta t}{2} \left[\{\Phi^n, g_m^n\} + ik_z \sqrt{\beta_i} \left(\frac{\sqrt{m+1}}{2} g_{m+1}^n + \frac{\sqrt{m}}{2} g_{m-1}^n \right) + \sqrt{\beta_i} \left\{ \Psi^n, \left(\frac{\sqrt{m+1}}{2} g_{m+1}^n + \frac{\sqrt{m}}{2} g_{m-1}^n \right) \right\} \right], \quad (2.17)$$

where the superscript denotes the time index.

2. Calculate nonlinear terms at the half time-step:

$$[\text{NL}]^{n+1/2} = -\frac{1}{2} \left[\{\xi^{+,n+1/2}, \nabla_{\perp}^2 \xi^{-,n+1/2}\} + \{\xi^{-,n+1/2}, \nabla_{\perp}^2 \xi^{+,n+1/2}\} \right. \\ \left. \mp \nabla_{\perp}^2 \{\xi^{+,n+1/2}, \xi^{-,n+1/2}\} \right]. \quad (2.18)$$

3. Take a full time-step using the nonlinear term calculated in the previous step:

$$\xi^{\pm,n+1} = e^{\pm ik_z \delta t} \xi^{\pm,n} + e^{\pm ik_z \delta t} \frac{1}{k_{\perp}^2} [\text{NL}]^{n+1/2}. \quad (2.19)$$

$$g_0^{n+1} = g_0^n - \delta t \left[\left\{ \Phi^{n+1/2}, g_0^{n+1/2} \right\} + \frac{ik_z \sqrt{\beta_i}}{\sqrt{2}} g_1^{n+1/2} + \sqrt{\beta_i} \left\{ \Psi^{n+1/2}, \frac{g_1^{n+1/2}}{\sqrt{2}} \right\} \right], \quad (2.20)$$

$$g_1^{n+1} = g_1^n - \delta t \left[\left\{ \Phi^{n+1/2}, g_1^{n+1/2} \right\} + ik_z \sqrt{\beta_i} \left(g_2^{n+1/2} + (1 - 1/\Lambda) \frac{g_0^{n+1/2}}{\sqrt{2}} \right) \right. \\ \left. + \sqrt{\beta_i} \left\{ \Psi^{n+1/2}, \left(g_2^{n+1/2} + (1 - 1/\Lambda) \frac{g_0^{n+1/2}}{\sqrt{2}} \right) \right\} \right], \quad (2.21)$$

$$\begin{aligned}
g_m^{n+1} = g_m^n - \frac{\delta t}{2} & \left[\left\{ \Phi^{n+1/2}, g_m^{n+1/2} \right\} + ik_z \sqrt{\beta_i} \left(\frac{\sqrt{m+1}}{2} g_{m+1}^{n+1/2} + \frac{\sqrt{m}}{2} g_{m-1}^n \right) \right. \\
& \left. + \sqrt{\beta_i} \left\{ \Psi^{n+1/2}, \left(\frac{\sqrt{m+1}}{2} g_{m+1}^{n+1/2} + \frac{\sqrt{m}}{2} g_{m-1}^{n+1/2} \right) \right\} \right]. \tag{2.22}
\end{aligned}$$

4. Integrate the dissipative terms (collisions and diffusion) using the same integrating factor technique as above:

$$\xi^\pm \rightarrow \xi^\pm \exp(-\eta k_\perp^2 \delta t), \tag{2.23}$$

$$g_0 \rightarrow g_0 \exp(-\eta k_\perp^2 \delta t), \quad g_1 \rightarrow g_1 \exp(-\eta k_\perp^2 \delta t), \tag{2.24}$$

$$g_m \rightarrow g_m \exp(-\eta k_\perp^2 \delta t - \nu m \delta t), \quad m \geq 2. \tag{2.25}$$

Since each Hermite moment is coupled to the next one, a suitable closure is required for the last retained Hermite moment, g_M . Two simple closures have been implemented: $g_{M+1} = 0$ and $g_{M+1} = g_{M-1}$. When the collisions are set high enough so that there is negligible energy in the last Hermite moment, the results are independent of the particular choice of closure. Throughout this thesis, we use the $g_{M+1} = 0$ closure, along with finite collisions.

Due to the explicit nature of the numerical scheme, the time step is restricted by a Courant-Friedrichs-Lowy condition:

$$\delta t = \frac{C}{\sqrt{M}} \times \text{Min} \left\{ \frac{1}{k_{x,\text{max}} \text{Max} \{ |k_y \xi^\pm| \}}, \frac{1}{k_{y,\text{max}} \text{Max} \{ |k_x \xi^\pm| \}} \right\}, \tag{2.26}$$

where C is a positive constant less than one, specified by the user.

2.5 Additional features

2.5.1 Forcing

A Gaussian white noise source has been implemented in order to study driven turbulence. The two Elsasser fields are driven using the same source—this ensures that only the velocity field $\mathbf{u}_\perp = \hat{\mathbf{z}} \times \nabla \Phi$ is forced, and there is no artificial large-scale reconnection. The slow modes are driven independently by forcing the zeroth and/or the first moment. The slow modes can also be driven by injecting energy into the field strength fluctuations—this physically corresponds to an external antenna that drives a perpendicular current in the plasma. The slow modes are driven at specified wavenumbers (k_x, k_y, k_z) [§].

2.5.2 Hyper-dissipation

Theories of turbulence generally give predictions for wavenumbers far from forcing and dissipation scales, *i.e.*, in the inertial range. The range of such wavenumbers may be estimated roughly as the ratio between the forcing and the dissipation scales, and hence is limited by resolution constraints. To maximize this range, we employ hyper-diffusion ($-\eta k_\perp^{2r}$) and hyper-collisions ($-\nu m^{2n}$) instead of regular diffusion ($-\eta k_\perp^2$) or collisions ($-\nu m$); r and n are positive integers. Such

[§]Due to the Alfvénic turbulence, the total magnetic field is not the same as the background magnetic field, $\mathbf{B} = B_0 \hat{\mathbf{z}} + \delta \mathbf{B}_\perp$. As a result, the wavenumber k_z is not necessarily same as the wavenumber along the total field k_\parallel . The implemented forcing routine does not check for what k_\parallel values are being forced.

hyper-dissipation operators restrict the dissipation range to a very narrow set of wavenumbers, and help the user simulate a large inertial range at a lower computational cost [82–86]. Typically, in this thesis, $r = 4$ and $n = 4$ were used. For the KRMHD simulations in Chapter 6, $r = 8$ was used.

2.5.3 Diagnostics

Gandalf writes out the following diagnostic data every few time-steps:

- For the Alfvénic fluctuations, we calculate the kinetic $|k_\perp^2 \Phi^2|$ and magnetic $|k_\perp^2 \Psi^2|$ energy spectra as functions of k_\perp and k_\parallel . For slow modes, the energy spectrum $|g_m^2|$ is a function of k_\perp , k_\parallel and m .

Energy at a particular perpendicular wavenumber $k_\perp = \sqrt{k_x^2 + k_y^2}$ is calculated by summing over shells. A mode at k_x, k_y contributes to the spectrum at k_\perp , if and only if, $k_\perp - 0.5 \leq \sqrt{k_x^2 + k_y^2} < k_\perp + 0.5$. The wavenumber k_\parallel , is the parallel wavenumber calculated along the local mean field. That is to say, k_\parallel includes the perpendicular perturbation:

$$\hat{\mathbf{b}} \cdot \nabla = \frac{\partial}{\partial z} + \{\Psi, \dots\}, \quad (2.27)$$

and is not same as k_z . The distinction between k_z and k_\parallel is important, because the two terms in Eq. (2.27) appear at the same order in the gyrokinetic ordering. Since particles are not aware of the split between the background and fluctuating magnetic fields, and always experience the total magnetic field, k_\parallel is the more physical choice for a parallel wavenumber. We calculate the

k_{\parallel} dependence of the spectra by following the exact field lines through our numerical box, and interpolating fluctuations along these field lines. This is done as follows:

1. Transform all the fluctuations from Fourier space to real space.
2. Pick an initial position x_0, y_0 at one end of the box, say $z_0 = -Lz/2$, where L_z is the length of the box in the z direction.
3. Calculate the perturbations $\mathbf{u}_{\perp} = \hat{\mathbf{z}} \times \Phi$, $\delta\mathbf{B}_{\perp} = \hat{\mathbf{z}} \times \Psi$ and g_m at $x = x_0, y = y_0, z = z_0$, using bilinear interpolation[¶].
4. Take a half step forward along the field line:

$$x_{1/2} = x_0 + \delta B_x \Delta z / 2, \quad y_{1/2} = y_0 + \delta B_y \Delta z / 2, \quad z_{1/2} = z_0 + \Delta z / 2, \quad (2.28)$$

where $\Delta z = L_z / k_{z,max}$ is the spacing-in- z between nearby grid points in real space.

5. Calculate the magnetic field perturbation $\delta\mathbf{B}_{\perp}$ at $x_{1/2}, y_{1/2}, z_{1/2}$ using bilinear interpolation.
6. Take a full step forward along the field line using the value of the magnetic field at $x_{1/2}, y_{1/2}, z_{1/2}$:

$$x_1 = x_0 + \delta B_x \Delta z, \quad y_1 = y_0 + \delta B_y \Delta z, \quad z_1 = z_0 + \Delta z. \quad (2.29)$$

[¶]This choice of interpolation scheme is sufficient for our purposes. A better scheme, like cubic splines could be easily implemented.

7. If $z_1 < L_z/2$, copy over the positions: $x_0 \leftarrow x_1$, $y_0 \leftarrow y_1$, $z_0 \leftarrow z_1$, and repeat from step 3.
8. Once the fluctuations \mathbf{u}_\perp , $\delta\mathbf{B}_\perp$ and g_m are known along the exact field lines, transform them back to Fourier space. The parallel wavenumber in this space is, in fact, k_\parallel .
9. Calculate the spectra as functions of k_\perp and k_\parallel by summing over shells, as discussed above.

A related, somewhat subtle issue is that of periodicity of the magnetic field lines. It is observed that the magnetic field lines that are initially periodic—say, for a driven simulation—naturally become aperiodic due to the turbulence. It can be shown that the $k_\parallel = 0$ mode plays a crucial role in giving rise to this aperiodicity. However, we do not discuss this point further in this thesis.

- The flux of energy $\Gamma_{m,\mathbf{k}}$ from the m^{th} to the $(m + 1)^{\text{st}}$ Hermite moment is calculated as

$$\Gamma_{m,\mathbf{k}} = -k_\parallel \sqrt{2(m + 1)} \operatorname{Im} [g_{m+1} g_m^*]. \quad (2.30)$$

The derivation of this expression is discussed in detail in Sec. 3.4.4.

- For large values of m , a slow mode perturbation can be split into a phase mixing component that propagates from small to large m , and an phase unmixing component that propagates from large to small m (see Sec. 3.4.5). In *Gandalf*, we also calculate the spectra for these phase mixing and phase unmixing modes.

2.6 Code verification

2.6.1 Kinetic fluctuation-dissipation relations

In Chapter 3, we calculate the saturated amplitudes of a driven kinetic field that evolves according to the linearized Vlasov equation. The analytical predictions are compared with the numerical results obtained from *Gandalf* in Figs. 3.1 and B.1. The comparison shows good agreement.

Fig. 3.3 plots the phase mixing and phase unmixing spectra of the kinetic field versus m . The numerical spectra calculated using *Gandalf* agree with the analytical prediction. The dotted lines in Fig. 3.3 are not fits to the numerical spectra, but are the exact expressions from Eqs. (3.37) and (3.58), *i.e.*, the agreement between the numerics and the analytical predictions is not just for the scaling in m , but also for the overall level of the spectra.

These comparisons provide a solid linear benchmark for *Gandalf*.

2.6.2 Orszag-Tang test case

We present results from the well-known Orszag-Tang test case [87] for MHD simulations. The initial condition for this test is given by

$$\Phi = -2 \left(\cos \left(2\pi \frac{x}{L_x} \right) + \cos \left(2\pi \frac{y}{L_y} \right) \right), \quad (2.31)$$

$$\Psi = \left(\cos \left(4\pi \frac{x}{L_x} \right) + 2 \cos \left(2\pi \frac{y}{L_y} \right) \right). \quad (2.32)$$

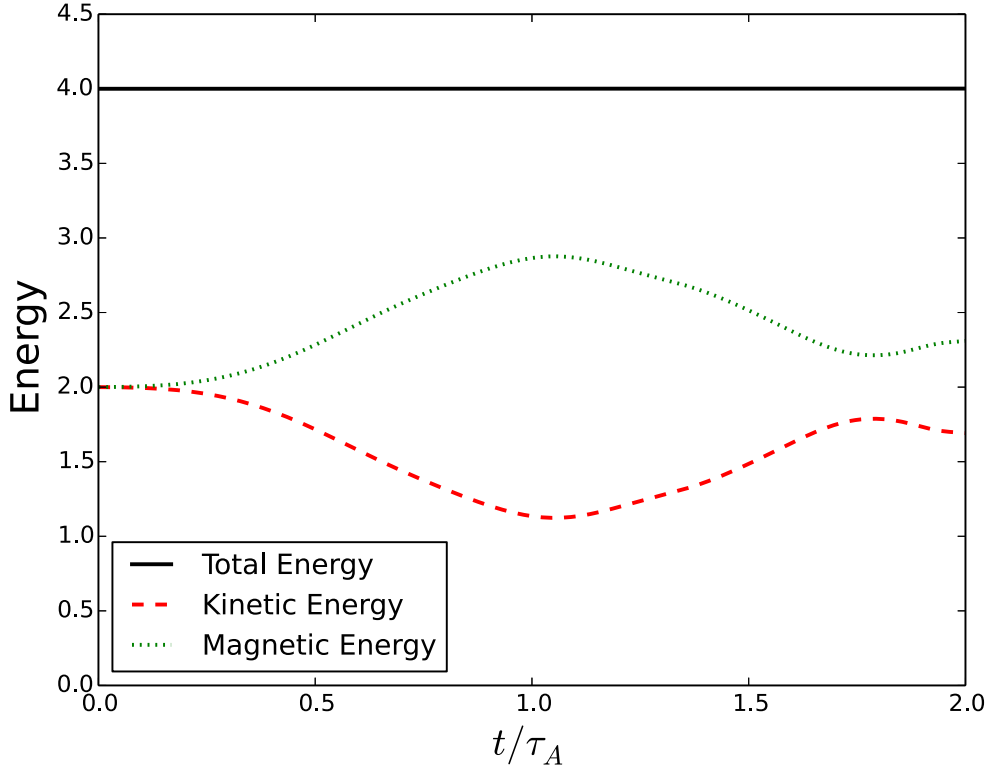


Figure 2.1: Time evolution of kinetic and magnetic energies for the Orszag-Tang test case.

We evolved this initial condition for two Alfvén times, using a $32^2 \times 1$ sized simulation domain. Fig. 2.1 plots the time evolution of kinetic and magnetic energies for the above initial condition, which is in qualitative agreement with the original results by Orszag and Tang.

2.6.3 Turbulent spectra for Alfvénic cascade

We simulated the reduced MHD equations for the simulation domains 64^3 , and 128^3 , with two different values for the hyper-diffusion exponent: $r = 4$ and $r = 8$. We ran these simulations till saturation, and then time-averaged the kinetic and magnetic energy spectra over two Alfvén times. These time-averaged spectra

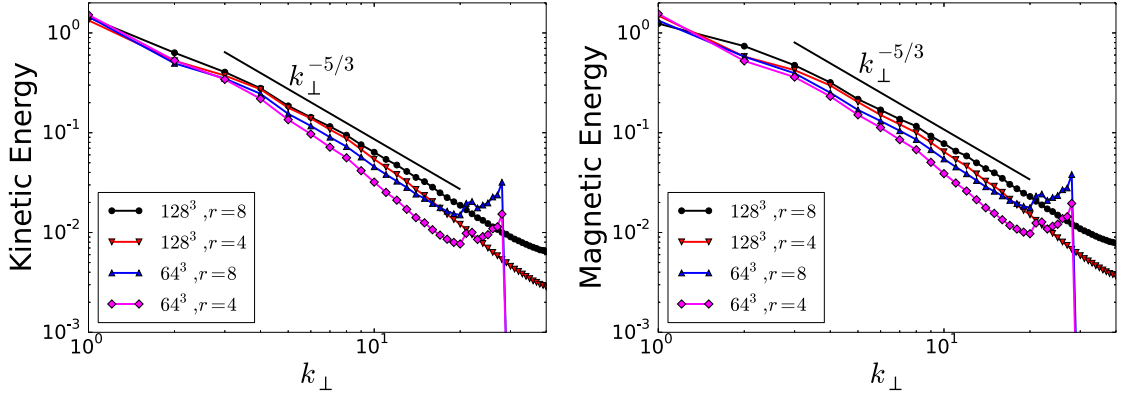


Figure 2.2: The kinetic (left) and magnetic (right) energy spectra for Alfvénic turbulent cascade. The four different lines correspond to four separate simulations—the first number is the resolution, and the second number is the exponent for the hyper-diffusion term (see Sec. 2.5.2). The spectra approach the critical-balance prediction of $k_{\perp}^{-5/3}$ for large resolution, and for large hyper-diffusion exponent.

are plotted in Fig. 2.2—they are in agreement with the critical-balance prediction of $k_{\perp}^{-5/3}$.